

pubs.acs.org/JPCC Article

Elucidating CO Oxidation Pathways on Rh Atoms and Clusters on the "29" Cu₂O/Cu(111) Surface

Published as part of The Journal of Physical Chemistry virtual special issue "Cynthia Friend Festschrift".

Alex C. Schilling, Nisa Ulumuddin, Volkan Çinar, Ryan T. Hannagan, Kyle Groden, Yicheng Wang, Laura A. Cramer, Paul L. Kress, Dipna A. Patel, Beverly Vo, Adrian Hunt, Phillip Christopher, Iradwikanari Waluyo, Jean-Sabin McEwen, and E. Charles H. Sykes*



ACCESS I

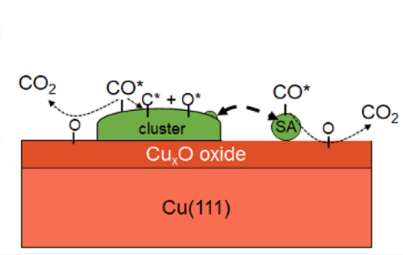
Cite This: J. Phys. Chem. C 2022, 126, 11091–11102

Metrics & More



Article Recommendations

co₂



ABSTRACT: Single-atom catalysts have attracted a great deal of attention due to their distinct reactivity and potential for cost savings. However, despite the wealth of literature in recent years, identifying the exact nature of the active sites and associated reaction mechanisms remains challenging in many cases. Herein, we take a surface science approach to understand how Rh single atoms and small clusters behave on the thin film "29" Cu₂O grown on Cu(111). We find that in contrast to Pt, which is present solely as single atoms on the "29" Cu₂O surface, Rh atoms and clusters coexist and each enable low-temperature CO oxidation, but via different pathways. Specifically, the single Rh atoms produce CO₂ at 444 K via a Mars van Krevelen mechanism whereas the Rh clusters can also dissociate CO₂ as demonstrated via isotope labeling, and liberate CO₂ at 313 K. Density functional theory (DFT) calculations quantify the energetics of these different pathways and demonstrate that only extended Rh is capable of CO dissociation. Low-temperature scanning tunneling microscopy (STM) reveals that unlike Pt atoms on the same surface, which stay atomically dispersed, the distribution of Rh structures is dependent on pretreatment conditions. DFT calculations reveal the greater tendency of Rh atoms to cluster than Pt, and STM image simulations confirm the active sites. Ambient pressure X-ray photoelectron spectroscopy studies on the same single crystal model systems demonstrate that 1% of a monolayer of Rh on the "29" Cu₂O thin film significantly accelerates its reduction by CO at 400 K, thus confirming the ultrahigh vacuum surface science findings. Together, these results illustrate how well-defined single crystal experiments are useful in building structure—function relationships that elucidate the reactivity of different ensemble sizes with a level of detail beyond what is possible with high surface area catalysis.

■ INTRODUCTION

Supported single-atom catalysts (SACs) have become a burgeoning area in catalysis research over the past decade. These systems combine the advantages of heterogeneous catalysts in terms of robustness and ease of product separation with the well-defined nature and high selectivity of homogeneous catalysts. The cost savings associated with dispersing the catalytic metal at the single atom limit is important given the increasing price of the precious metals used in many catalytic processes. Previous studies have demonstrated that both single atom sites and supported nanoparticles can catalyze a variety of industrially relevant reactions. Pala Relevant to this work, it has been proposed that isolated Rh sites can catalyze C–H bond activation, CO

oxidation, NO reduction, and the WGS reaction without any methanation. 9,10,14

However, despite the wealth of literature on supported catalysts, identifying the exact nature of the active site and the reaction mechanism remains challenging. To probe these questions in more detail, model single crystal systems are very

 Received:
 April 19, 2022

 Revised:
 June 10, 2022

 Published:
 June 29, 2022





Supporting Information

useful in enabling the atomic scale structure of the active sites to be probed and directly related to reaction chemistry. $^{15-18}$ Previous studies on a variety of supports have shown that isolated sites behave differently than nanoparticles. 12,16,19,20 Furthermore, adsorbate-induced restructuring of the active sites, as well as strong metal—support interactions, complicates the picture. For example, Solymosi et al. found that adding CO to Rh/Al₂O₃ leads to the dispersion of Rh particles; however, when heated the Rh particles tend to agglomerate. 13 Other researchers have also found CO to play a part in the sintering or dispersion of Rh active sites throughout the catalytic process.

The ability of both single atom Rh sites and Rh nanoparticles to catalyze CO oxidation, coupled with the fact that CO is known to affect the dispersion of the Rh, makes it difficult to distinguish the exact role of these two types of active sites. The dynamic nature of these types of systems has been modeled by Rousseau et al. on Au/ceria as a model catalyst for CO oxidation. The authors propose a mechanism by which dynamically exposed Au atoms that strongly couple with the ceria support were responsible for CO oxidation, after which they could return to the Au nanoparticle where they originated from. While detailed modeling can uncover such potentially important catalytic phenomena, it is very difficult to attain such a full understanding in experimental systems, especially ones in which the active sites change dynamically in response to the reactants.

In this study we employ a combined model catalyst and theoretical approach to understand the reactivity of a range of coverages of Rh on a well-defined thin film Cu₂O support. This so-called "29" Cu₂O thin film grown on Cu(111) has been used previously to model supported single-site catalysts and has a unit cell consisting of six hexagonal -(O-Cu)- rings, five of which contain an oxygen adatom. The "29" Cu₂O unit cell is 29 times larger than the underlying Cu(111) unit cell, hence the term "29" Cu₂O thin film. 21,22 The current work focuses on the ability of low loadings of Rh on this Cu₂O thin film to oxidize CO. Surface sensitive techniques that include scanning tunneling microscopy (STM), temperature-programmed desorption (TPD), and X-ray photoelectron spectroscopy (XPS) enable us to investigate the atomic-scale structure and reactivity of this well-defined catalytic model system and to decouple the reactivity of single Rh atoms and clusters, which are present on the oxide thin film. Throughout this paper, we compare the Rh on the "29" oxide results to previously published data for Pt on the same oxide surface.²² In that study, it was found that low coverages of Pt on the "29" Cu₂O oxide were present exclusively as single atoms that were capable of converting ~33% of adsorbed CO to CO₂ at ~350 K with the remainder of the CO desorbing unreacted around the same temperature. By comparing and contrasting the behavior of Rh with Pt, we find several important differences which are understood with theoretical modeling. Specifically, we find that at all surface coverages studied, Rh is present on the "29" Cu₂O as both single atoms and clusters, both of which are able to oxidize CO to CO2 which evolves at two distinct temperatures that are characteristic of the active site being single Rh atoms or clusters. Using isotope labeling studies and DFT modeling we elucidate the different reaction pathways on Rh single atoms and clusters as well as compare and contrast the CO oxidation mechanism with what is known for Pt on the same support.

METHODS

TPD. TPD experiments were performed in an ultrahigh vacuum (UHV) chamber with a base pressure $<1 \times 10^{-10}$ mbar. This chamber has a Hiden Hal/3F 301 RC quadrupole mass spectrometer, and the Cu(111) crystal could be resistively heated to 750 K and cooled with liquid nitrogen to 85 K. The crystal was cleaned thoroughly by repeated Ar⁺ sputtering and 750 K annealing cycles. The "29" Cu₂O thin film was formed by exposure to either ¹⁶O₂ (USP grade; Airgas) or ¹⁸O₂ (97% isotopic purity; Aldrich) for 3 min at a pressure of 5×10^{-6} mbar while the sample was held at $550 \pm$ 20 K. The structure of the "29" oxide was confirmed via CO TPD as described by Hensley et al.²³ Rh deposition was performed with the sample held at 85 K using a flux-monitored Focus GmbH EFM3 electron beam evaporator. These Rh coverages were calibrated with CO titration experiments of the same Rh dose on the Cu(111) crystal from which CO desorbs intact at low Rh coverage.²⁴ Monolayer assignments are based on the packing density of Cu(111) of 1.77×10^{15} atoms/ cm^{2,25} All TPD experiments of CO (99.99%; Airgas) were performed with a 1 K/s linear heating rate. Quantitative analysis of TPD peaks included correction factors for the quadrupole mass spectrometer sensitivity, as well as the fragmentation pattern and ionization cross section of the desorbing molecule of interest.

STM. The samples used in STM experiments were made in a preparation chamber (base pressure $<2\times10^{-10}$ mbar) using the same conditions as outlined in the TPD experiments except for the oxygen deposition which occurred at 650 K but lead to the formation of the same "29" oxide. The prepared samples were transferred under UHV to the STM chamber (base pressure $<1\times10^{-11}$ mbar) containing a precooled 5 K Omicron Nano Technology STM. CO was deposited on the sample at 5 K using a line-of-sight high precision leak valve, and the sample was annealed to various temperatures prior to cooling back down to 5 K for imaging. The STM images were obtained with etched W tips, and typical imaging conditions of -0.5 V with respect to the sample and tunneling currents \sim 0.5 nA were used.

XPS. UHV and ambient pressure (AP-) XPS experiments were performed at the In situ and Operando Soft X-ray Spectroscopy (IOS, 23-ID-2) beamline at the National Synchrotron Light Source II (NSLS-II), Brookhaven National Laboratory. A description of the beamline and endstation can be found elsewhere. 26 The Cu(111) crystal was cleaned by repeated cycles of Ar⁺ sputtering and 850 K annealing until the C and O contamination peaks were no longer detectable by XPS. The "29" Cu₂O film was prepared by exposing the sample to 5×10^{-6} Torr of O₂ (Matheson, ultrahigh purity, 99.98%) at a sample temperature of 650 K for 3 min. Rh was evaporated at a sample temperature of 300 K using a SPECS EBE-4 electron beam evaporator, and the evaporation rate was calibrated with a quartz crystal microbalance. Exposures to CO (Matheson, research purity, 99.999%) were done at either 300 or 400 K. Rh 3d and C 1s core levels were measured with a photon energy of 500 eV, and O 1s was measured with a photon energy of 710 eV. The binding energy was calibrated to the Fermi level measured at each photon energy.

Density Functional Theory. All theoretical simulations were conducted using the Vienna *Ab initio* Software Package (VASP). To model the electronic orbitals, a planewave basis set was used, where the Projector Augmented Wave

(PAW) potentials released in 2015^{29} modeled the core orbitals to be frozen.³⁰ Based on the PAW potentials, the Cu $3p^6$, $3d^{10}$ and $4s^1$, O $2s^2$ and $2p^4$, and Rh $4d^8$ and $5s^1$ electrons make up the valence states. The planewave basis had a kinetic cutoff energy of 500 eV with a Gaussian smearing of 0.2 eV at the Fermi level.

The "29" oxide surface was modeled using the structurally accurate "29" oxide model published by Therrien et al.²¹ Density Functional Theory calculations were performed within the generalized gradient approximation (GGA) using the Perdew, Burke, and Erzenhof (PBE) exchange-correlation functional.³¹ All calculations involved here were spin-polarized, although the resulting magnetic moment of the structures are 0. Structurally, the "29" oxide model consists of an atomic film of Cu_xO rings resting on top of a Cu(111) facet. 21 Its unit cell comprises 6 Cu_xO rings with an O adatom within 5 of these rings. The underlying Cu(111) substrate follows a periodicity of its $\sqrt{13}$ R46.1° × 7R21.8° supercell, approximately 29 times larger than its $p(1 \times 1)$ unit cell. The "29" oxide unit cell has a surface area of $18 \times 19 \text{ Å}^2$. During all geometry optimizations, the two bottom layers of Cu(111) were fixed in their bulk positions, while the top two Cu(111) layers and the rest of the atoms were relaxed. To minimize "charge sloshing" between periodic cells, a vacuum layer of 15 Å height was set on top of the slab.³² As determined by Therrien et al., an optimal k-point sampling of $1 \times 2 \times 1$ using the Monkhorst-Pack³³ grid was used to sample the Brillouin zone. The clean "29" oxide unit cell is shown in Figure 1.

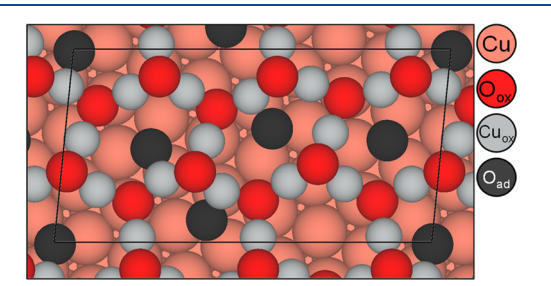


Figure 1. DFT model of the "29" oxide unit cell. The atoms are color coded: Cu (pink), oxide-O (red), oxide-Cu (gray), adatom-O (black).

To model the active site of CO dissociation on Rh clusters, a Rh(211) facet was used because the lower coordination sites on the 211 facet provide a better model of the clusters that exhibit more reactive undercoordinated sites than a typical 111 facet. Calculations here were not spin polarized. Supercells of $p(2 \times 2)$ and $p(2 \times 3)$ were used to ensure that the adsorbed CO is spatially isolated from its periodic image during the simulation of its CO oxidation and analysis of its electronic structure. To sample the Brillouin zone, Monkhorst–Pack kpoints grids of $(1 \times 2 \times 1)$ and $(1 \times 1 \times 1)$ were applied to the $p(2 \times 2)$ and $p(2 \times 3)$ supercells, respectively. The same vacuum slab thickness as the "29" oxide model was also applied in both models. Both slabs consist of 6 atomic layers, where the top 3 layers are relaxed and the bottom 3 layers are fixed.

All geometry optimization calculations were set to converge after the energy and force criteria reach 10^{-6} eV and 10^{-2} eV/Å respectively. The transition states were calculated using the climbing nudged elastic band (CI-NEB)³⁴ method and was set to converge after the total energy and interatomic force differences reach 10^{-5} eV and 10^{-2} eV/Å respectively. To ensure that the highest energy is at the saddle point, a vibrational states calculation ensuring the existence of only a single imaginary mode along the reaction pathway was conducted.³⁵

The adsorption energy of CO on the two model surfaces were calculated according to

$$E_{\rm ads} = E_{\rm CO/slab} - E_{\rm slab} - E_{\rm CO(g)} \tag{1}$$

where $E_{\rm CO/slab}$, $E_{\rm slab}$, and $E_{\rm CO(g)}$ are the total energies of CO-adsorbed surface, the clean surface, and CO in the gas phase, respectively.

To investigate how much the CO electronic structure changes by bonding with the surface, we calculated the ratio of filled and unfilled states:

$$\frac{F}{U} = \frac{\int_{-\infty}^{E_{\text{Fermi}}} \rho(E) \, dE}{\int_{E_{\text{Fermi}}}^{\infty} \rho(E) \, dE}$$
(2)

where E is the energy level, $\rho(E)$ is the density of electronic states at a given energy, and E_{Fermi} is the Fermi energy. A higher ratio correlates to a higher possibility that more

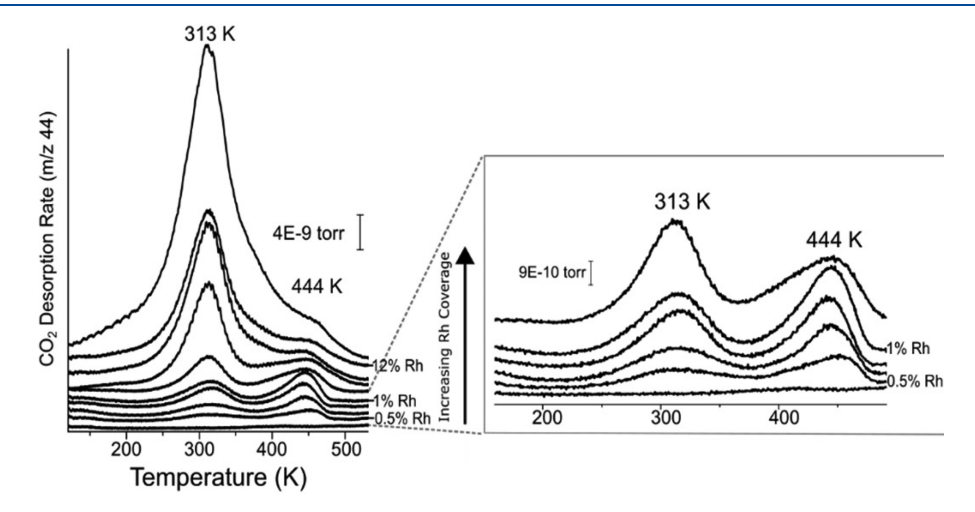


Figure 2. TPD traces showing CO oxidation activity as a function of Rh coverage. Left panel shows TPD curves of CO₂ desorption from the Rh/Cu₂O surface over a range of Rh coverages (0%, 0.5%, 0.75%, 0.9%, 1%, 1.8%, 4%, 9.5%, 12%, and 24% of a monolayer of Rh). Right panel shows magnified CO₂ desorption traces from the lower Rh coverages.

antibonding states within CO are filled by rehybridizing with the surface states.

RESULTS AND DISCUSSION

We began the study by testing the ability of the Rh on "29" Cu_2O model system to oxidize CO as a function of Rh coverage on the surface as seen in Figure 2 and also image the surface with STM as shown in Figure 3. Figure 2 shows a series

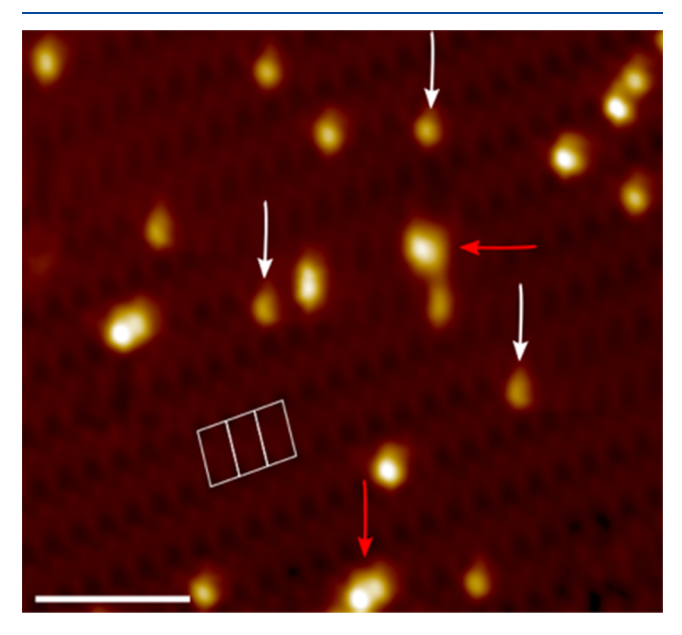


Figure 3. STM image showing 1% of a monolayer of Rh on the "29" Cu_2O surface after exposure to saturation CO and annealing to 200 K to remove CO from the oxide surface. White arrows highlight the atomically dispersed Rh sites, and the red arrows highlight Rh clusters. Three unit cells of the "29" oxide are outlined in white. Scale bar is 5 pm.

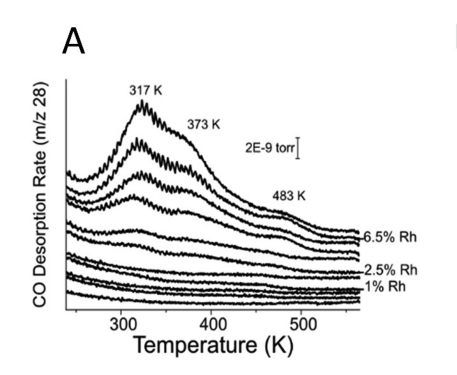
of CO oxidation TPD data taken after saturation CO (10 L, where 1 Langmuir = 1×10^{-6} Torr·s) was deposited onto a range of Rh coverages on the "29" oxide. When no Rh is present on the "29" oxide, all the CO desorbs below 200 K.²³ However, Figure 2 shows that when low coverages of Rh are deposited on the "29" oxide and exposed to saturation CO, we observe two distinct CO₂ desorption features above 300 K and no CO desorption, as seen in Figure 4A. This result is significant in demonstrating that, unlike low coverages of Pt on

the "29" oxide which convert only 33% of the adsorbed CO to CO_2 , at low Rh coverage every Rh site can facilitate the oxidation of adsorbed CO to CO_2 as seen by the lack of CO desorption in the TPD traces shown in Figure 4. Furthermore, unlike low coverages of Pt, which exhibit only one CO_2 desorption peak ~ 350 K, two CO_2 desorption peaks appear at 313 and 444 K for Rh as seen in Figure 2. Below 2% Rh coverage, the low and high temperature peak areas maintain a roughly 1:1 ratio. Then, as the Rh coverage increases above 2%, the low temperature CO_2 desorption peak becomes the dominant feature and the high temperature peak is just a small shoulder on the low temperature CO_2 desorption peak as seen in Figure 2.

In order to investigate the origin of this CO oxidation reactivity, we imaged low coverages of Rh on the "29" $\mathrm{Cu_2O}$ surface with 5 K STM. Unlike Pt on the "29" oxide surface which forms exclusively single atom active sites, 22 when low loadings of Rh are deposited on the "29" oxide surface, we observed a variety of surface species including single atoms and various sizes of clusters as highlighted by the white and red arrows respectively in the STM image shown in Figure 3. This image was taken after a $\mathrm{Cu}(111)$ sample was covered with the "29" oxide and 1% of a monolayer of Rh was deposited on the surface. The sample was then saturated with CO and annealed to 200 K, to ensure the CO had desorbed off the oxide layer, and then imaged at 5 K.

This STM result provides evidence for the existence of both atomically dispersed Rh sites and small clusters on the "29" oxide surface at low Rh coverages and is consistent with the appearance of two CO_2 peaks in Figure 2. We therefore postulate that the higher temperature CO_2 peak originates from CO oxidation at the atomically dispersed Rh sites and the lower temperature peak from Rh clusters. The fact that higher Rh loadings on the "29" oxide led to a larger low-temperature CO_2 peak is consistent with this hypothesis given that higher Rh coverages will lead to the formation of more clusters.

Figure 4 shows that at Rh coverages greater than 2% we begin to observe that not all of the CO bound to Rh sites is oxidized to CO₂. Specifically, the appearance of a CO desorption peak in the 317–373 K region becomes prominent at Rh coverages greater than 5% of a monolayer, related to Rh clusters being present at the higher coverages which have less access to surface oxygen for the CO oxidation step, and the CO remains trapped on the Rh cluster until it can desorb as CO at higher temperatures. In order to investigate the CO oxidation mechanism and demonstrate that the oxygen is



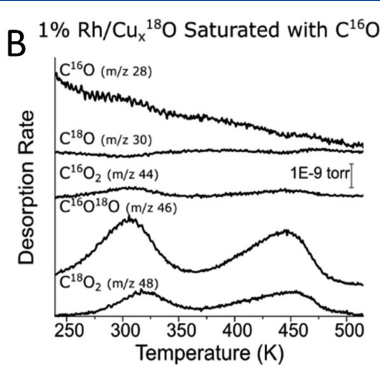


Figure 4. (A) TPD traces for CO desorption from various coverages (0%, 0.25%, 0.5%, 0.75%, 1%, 1.8%, 2.5%, 3.5%, 4%, 5%, 6.5%, 12%) of Rh on the "29" oxide. (B) Isotope labeling experiment in which the "29" oxide surface was made with 18 O, and CO and CO₂ with a range of m/z ratios corresponding to the different isotopes are observed desorbing after the adsorption of C^{16} O.

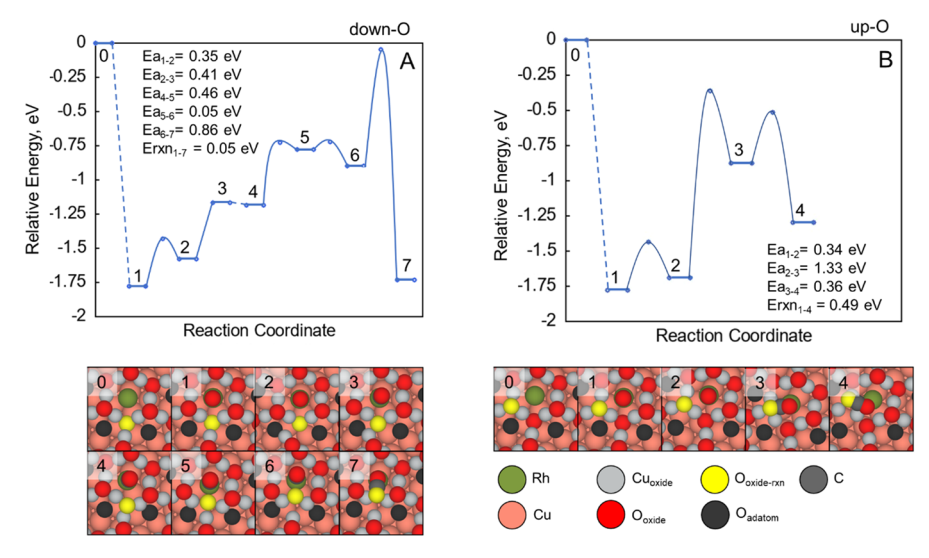


Figure 5. CO oxidation pathway from atomically dispersed Rh from a representative (A) down-O and (B) up-O of the "29" oxide. Solid lines display steps with calculated transition state energies. Dashed lines indicate that no transition state calculation was done. E_a = activation energy, E_{rxn} = reaction energy.

supplied from the "29" oxide itself, we performed isotopic labeling studies as shown in Figure 4B. In these experiments, the "29" oxide was grown using 18O2, Rh was deposited in the usual manner, and the evolving CO and CO2 were measured in the TPD experiment at a variety of m/z ratios that correspond to the differently labeled molecules. The TPD traces in Figure 4B show that with 1% of a monolayer of Rh on the ¹⁸O-labeled "29" oxide, CO_2 is seen desorbing with different m/z ratios. The main CO_2 product is observed at m/z = 46 corresponding to C16O18O which is formed through the Mars-van Krevelen mechanism, ²⁵ occurs when a C¹⁶O molecule adsorbs to a Rh site, extracts an oxygen atom from the ¹⁸O-labeled "29" oxide surface, and desorbs as C16O18O. This same mechanism was responsible for all the CO2 production from CO oxidation on atomically dispersed Pt on the "29" oxide surface. 22 We will address the other two CO2 isotopes observed later in the

To understand why higher CO conversion and higher CO₂ desorption temperatures were observed on the Rh "29" oxide system as compared to the Pt "29" oxide system, we calculated the reaction barriers involved in the oxidation of CO adsorbed on atomically dispersed Rh sites within our DFT-based model. As shown in Figure S1, we first compared the reaction energies of CO combining with all possible "29" oxide O atoms surrounding the Rh site. There are two representative positions of oxide-O, the up-positions (up-O) and the down-positions (down-O). Generally, the CO oxidation reaction energies with a down-O are either slightly endothermic or slightly exothermic (-0.16-0.13 eV). In contrast, the corresponding energies with an up-O are more endothermic (0.48–0.59 eV). We then selected the lowest reaction energies from the two cases, and the energetic barriers involved in the reaction were calculated and shown in Figure 5. Here, our energies are zeroed at the clean atomically dispersed Rh site with CO in the gas phase. Upon the adsorption of CO, the energy of the system changes by -1.78 eV. We can see that not only the bonding with down-O is thermodynamically more favorable upon CO adsorption but also the activation barrier of its rate limiting step is 0.86 eV ($E_{a_{6-7}}$), which is 0.47 eV lower than the rate-limiting step of oxidation with up-O (E_{a_1}) , making it the

minimum energy pathway (MEP). For both cases, the rate-limiting step consists of the formation of $\rm CO_2$ adsorbed on the single Rh atom site. While the oxidation of CO involves only one elementary step (step 6–7 for down-O, and step 2–3 for up-O), our DFT simulations found many intermediate ground states where the oxide ring and the Rh-CO entity reposition themselves to the most favorable configurations first.

We can gain many insights from comparing the energetics of CO oxidation on Rh single atoms to CO oxidation on Pt single atoms on the same "29" oxide surface as calculated previously.²² First, the activation barrier on Rh within the MEP (Figure 5A) is ~0.36 eV higher than that for Pt on the "29" oxide. 22 This is in support of our observation that the CO oxidation peak associated with Rh single atoms (444 K) is at a higher temperature than the peak associated with CO oxidation on Pt single atoms (350 K).²² We have also previously observed that only 33% of CO adsorbed to isolated Pt atoms was oxidized on the Pt-deposited "29" oxide while 100% of the CO reacted on the low coverage Rh-deposited systems. Our DFT calculations indicate that the adsorption of CO on a Rh single atom is exothermic at -1.78 eV. Although the activation barrier to oxidation is high at 0.86 eV, as shown in Figure 5A, the Rh-CO bond is strong enough (0.90 eV) to hinder CO desorption. We also note that step 6-7 in Figure 5A is highly exothermic. The energetic landscape is slightly different in the case of Pt. First, the adsorption of CO on the Pt single atom is -1.27 eV, which is ~ 0.5 eV weaker than its adsorption on Rh.²² Second, the reaction energy to convert CO to CO₂ is thermodynamically nearly isoenergetic. Therefore, the desorption of CO from atomically dispersed Pt is comparably easier than its desorption from atomically dispersed Rh, resulting in the lower conversion rate being observed experimentally on the Pt system.

Unlike Pt on the "29" oxide which forms $C^{16}O^{18}O$ exclusively, $C^{18}O_2$ is also observed desorbing from the Rhdoped "29" oxide. To form $C^{18}O_2$, CO bond scission must occur so that the C atom of the as-deposited $C^{16}O$ can separate from the ^{16}O and bind to two ^{18}O atoms from the oxide surface. Consistent with this postulate, small amounts of $C^{16}O_2$ are also seen desorbing from the sample as seen in Figure 4B. Specifically, for $C^{16}O_2$ to form, the deposited $C^{16}O$ must pick

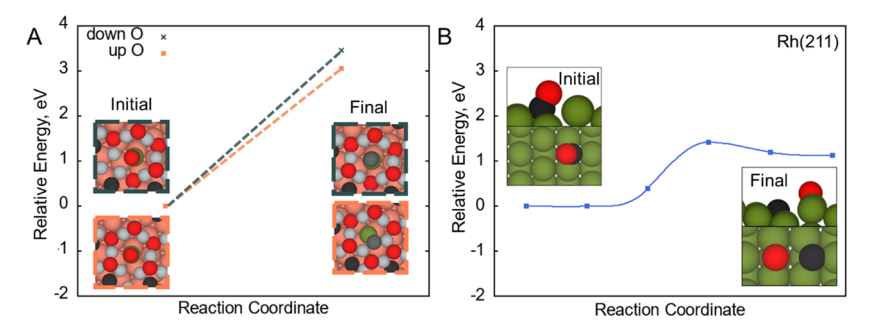


Figure 6. (A) Reaction energies for CO dissociation on Rh_1 on the "29" oxide in the presence of an oxygen vacancy considering two scenarios: bonding CO_{ads} with down- O_{oxide} and up- O_{oxide} . (B) The reaction barrier of CO dissociation at a B_5 site on Rh(211). The color scheme for the species is the same as that in Figure 5.

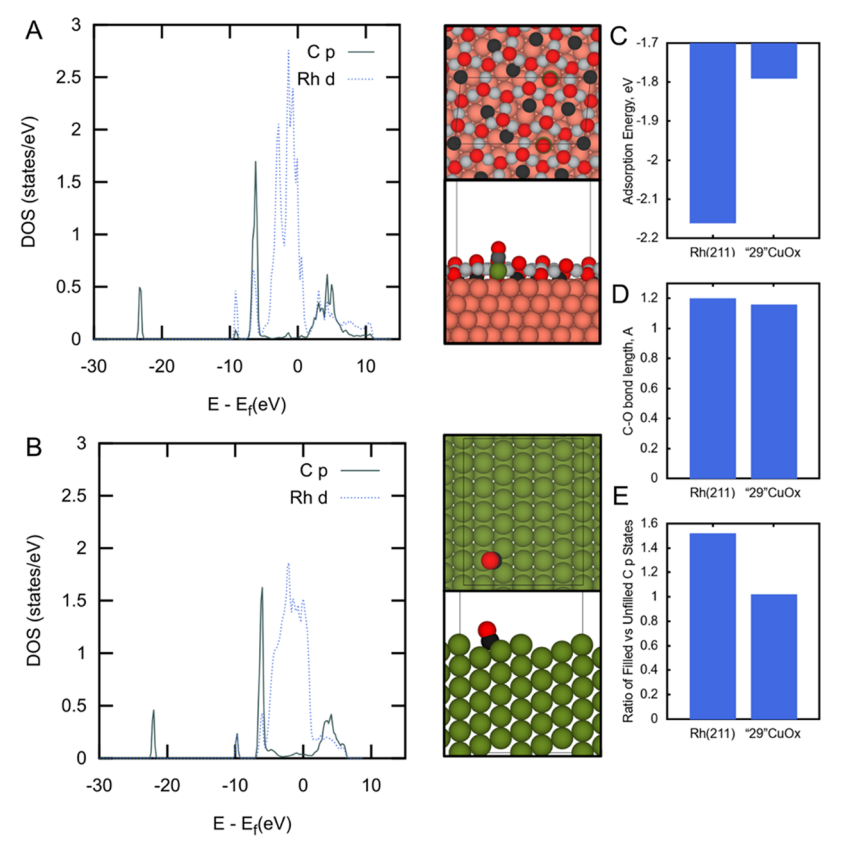


Figure 7. Density of states of the C p-states (solid line) of CO_{ads} and Rh d-states (dotted line) of the Rh with CO_{ads} when (A) atomically dispersed on the "29" oxide and (B) on a Rh(211) stepped surface. The comparison of (C) CO adsorption energy (D) C–O bond length and (E) the ratio of the filled vs the unfilled C p-states for the Rh₁/"29" oxide and the Rh(211) model systems. The color scheme is the same as Figure 5.

up an ¹⁶O from the surface. However, because the "29" oxide in these experiments was made with ¹⁸O, the only ¹⁶O present must originate from dissociation of the C¹⁶O deposited on the surface, thus providing further evidence for CO dissociation on the Rh-covered "29" oxide that was not observed for the case of Pt. Furthermore, the product ratio for the different types of CO₂ desorbing from the Rh-covered "29" oxide (C¹⁶O¹⁸O:C¹⁸O₂:C¹⁶O₂) was 12:5:1 after accounting for background CO scrambling on the chamber walls. This is consistent with the major pathway involving the Mars—van Krevelen mechanism in which the deposited C¹⁶O reacts with surface ¹⁸O to form C¹⁶O¹⁸O and a minor pathway involving CO dissociation.

CO dissociation is known to be a surface structure sensitive reaction, as its reaction rate strongly depends on the catalyst

particle size and its surface geometry. The known active sites for CO dissociation on Rh have been discussed in the literature, $^{36-39}$ and DFT studies have determined that the lowest activation barrier is facilitated at B sites of Rh(211) facets. We performed calculations within our DFT-based model to compare results on Rh(211) to the energy cost for dissociating CO on atomically dispersed Rh atoms (Rh₁) when deposited on the "29" oxide in the presence of an oxygen vacancy. Specifically, on single atom Rh sites we hypothesize that the presence of an oxygen vacancy would be necessary for the CO dissociation process to occur. As shown in Figure 6, the dissociated O from CO $_{\rm ads}$ can arrive at two representative O $_{\rm oxide}$ positions on the "29" oxide, namely down-O and up-O. These positions correspond to the direction of the $-({\rm Cu}-{\rm O})-{\rm zigzag}$ structure. We found that the energetic cost to

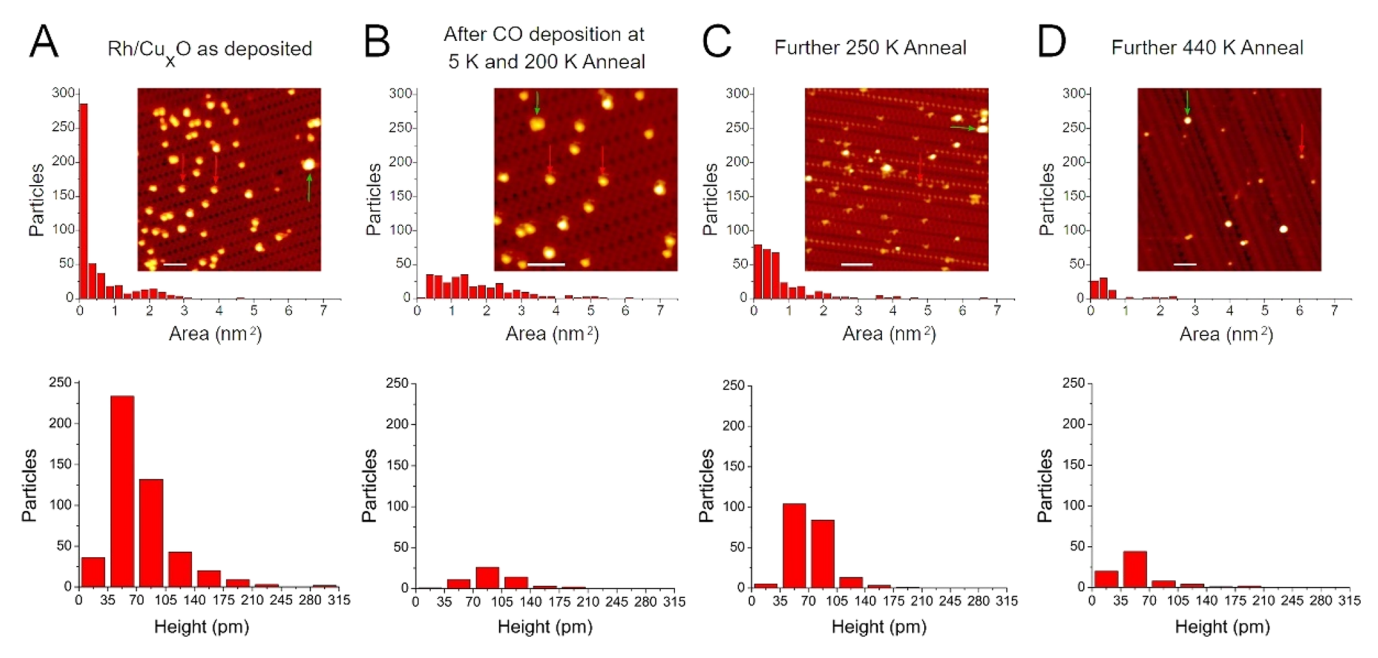


Figure 8. STM images and particle area and apparent height histograms of Rh on the "29" oxide after various annealing steps and CO deposition. (A) 1% of a monolayer of Rh on the "29" oxide imaged at 5 K, (B) same sample after CO exposure and 200 K anneal to remove CO from the oxide, (C) 250 K anneal, and (D) after a 440 K anneal. All scale bars are 5 nm. The red arrows show atomically dispersed Rh, and the green arrows show Rh clusters.

dissociate CO on Rh_1 is highly endothermic, with a reaction energy of 3.05 eV (up-O) or 3.46 eV (down-O). In contrast, the energy barrier for CO dissociation at the B_5 site of Rh(211) is only 1.42 eV, comparable to the value calculated by Filot et al.³⁶ Our results indicate that it is highly likely that Rh clusters on the "29" oxide provide the necessary sites for CO dissociation that leads to the scrambling observed in the CO_2 product, whereas the single atom Rh_1 sites do not dissociate CO due to the high barrier.

In order to compare how CO binds to an atomically dispersed Rh₁ on the "29" oxide and at the B₅ site of a Rh(211) facet, we compared the projected density of states (PDOS) of the C p-states as well as the interacting Rh d-band for both models as shown in Figure 7A and B. Unsurprisingly, the dstates of the atomically dispersed Rh have more discrete peaks than the d-band of the Rh(211) surface. This is due to the Rh having less of a metallic character when atomically dispersed on the "29" oxide. Despite the stark difference in CO adsorption energies (Figure 7C), the rehybridized C p-states of the two systems qualitatively look indistinguishable from each other. A more quantitative analysis is shown in Figure 7E, where the stronger adsorption on Rh(211) is reflected by a higher ratio between the filled and unfilled C p states. The Rh(211) surface rehybridizes CO so strongly that more CO antibonding states are filled, weakening the C-O bond. This high interaction strength was not found when CO bonds to the atomically dispersed Rh on the "29" oxide. As a result, the internal C-O bond length when adsorbed on the Rh(211) surface is longer than when it binds to the atomically dispersed Rh on the "29" oxide by 0.05 Å, as shown by Figure 7D.

Interestingly, Figure 4B reveals that $C^{18}O_2$, which derives from CO that has dissociated and recombined with two "29" oxide ^{18}O atoms, is evolved from both Rh clusters and Rh single atoms at ~ 320 K and ~ 450 K respectively. While at first inspection this would infer that both Rh clusters and Rh atoms dissociate CO to the same degree, our DFT-based model

calculations just described indicate that the barrier to CO dissociation on atomically dispersed Rh is prohibitively high, providing evidence for transport of CO between the different active sites. Specifically, CO can dissociate on Rh clusters, recombine, and form CO₂, whereas the single Rh atoms cannot dissociate CO. Therefore, $C^{18}O$ that has been isotopescrambled at Rh clusters can mix with CO at the Rh singleatom sites, by either diffusion of CO or the Rh itself, and become further oxidized to $C^{18}O_2$, consistent with our observation of doubly labeled $C^{18}O_2$ evolving from both Rh site types.

Rh Mobilization on the Oxide Support. To visualize how the Rh sites and the oxide support evolve throughout the CO oxidation reaction, 1% of a monolayer of Rh was deposited on the "29" oxide sample and imaged at 5 K before depositing CO and annealing it to progressively higher temperatures (200, 250, and 440 K) in order to examine the atomic scale structure of the surface before and after each CO_2 desorption peak seen in the TPDs in Figures 2 and 4.

Figure 8A shows a 5 K STM image of 1% of a monolayer of Rh deposited on a pristine "29" oxide surface. This image demonstrates that a mix of Rh single atoms and clusters (as indicated by the red and green arrows, respectively) is present on the surface. A series of images of the surface were taken after the different pretreatments indicated, histogram plots of the area the Rh ensembles occupy, and the apparent height of the Rh ensembles are given in Figure 8. From the Rh ensemble area histogram, we see that, as deposited, a large number of the Rh species occupy an area 0-0.25 nm² and an apparent height ~50 pm, consistent with the presence of atomically dispersed Rh sites before exposure to CO. The assignment of these smallest features in the STM images to single atoms is verified by the identical apparent height and area of these sites as highlighted by the red arrows. Furthermore, unlike Pt on the "29" oxide which only exists as single atoms, we also observe a

variety of Rh cluster sizes with areas ranging from 0.5 to $3.25 \, \text{nm}^2$.

After exposing this sample to saturation 10 L of CO, we annealed the surface to 200 K to desorb the CO from the "29" oxide layer, and the sample was imaged again at 5 K as shown in Figure 8B. The first noticeable difference between the sample before and after CO exposure is that after CO exposure, there are much fewer Rh species in the size range 0-0.25 nm² attributed to atomically dispersed sites and more of the Rh being present as clusters. Consistent with this we also see an increase in the apparent height of the sites to ~ 100 pm. The sample was then annealed to 250 K, at which temperature the CO should have been oxidized on the Rh clusters. This is because the leading edge of the low temperature CO₂ desorption peak extends below 250 K, so annealing to 250 K is enough to oxidize the CO on the clusters. After this 250 K anneal, defects in the oxide layer appear in the STM images consistent with the predominant Mars-van Krevelen oxidation pathway in which O atoms are removed from the pristine "29" oxide surface leaving O vacancies that appear as depressions.²² The cluster size distribution histogram for the sample after the 250 K anneal shows that after the low temperature CO₂ desorption peak, there are more clusters in the 0-0.25 nm² range attributed to dispersion of some of the clusters back into single sites with apparent heights of ~50 pm as seen in the histogram. The prevalence of atomically dispersed sites at this stage of the reaction also corroborates our claim that the high temperature CO₂ peak in our TPD traces stems from CO₂ desorption from Rh atoms. Upon heating the sample further to 440 K as seen in Figure 8D, we see a dramatic reduction in the number of Rh clusters visible on/under the surface and those that remain measure between 0 and 0.75 nm². This provides further evidence of the redispersion of Rh clusters to atomically dispersed sites, and it also indicates that after this 440 K anneal, the majority of the Rh atoms reside beneath the "29" oxide where they are not visible in the STM images. This movement of surface-bound atoms under the oxide at higher temperature was also observed for Pt on the "29" oxide.

Within our DFT-based model, we have simulated two hypothetical scenarios of the aggregation of Pt and Rh into dimers on the "29" oxide, where two dopant metals isolated in two oxide rings combine to form a dimer as shown in Figure 9. Figure 9 provides validation that the formation of Rh dimers is energetically more favorable than the formation of Pt dimers. We also see that the oxide rings around the Rh adatoms more easily break and locally reconstruct. This effect was not

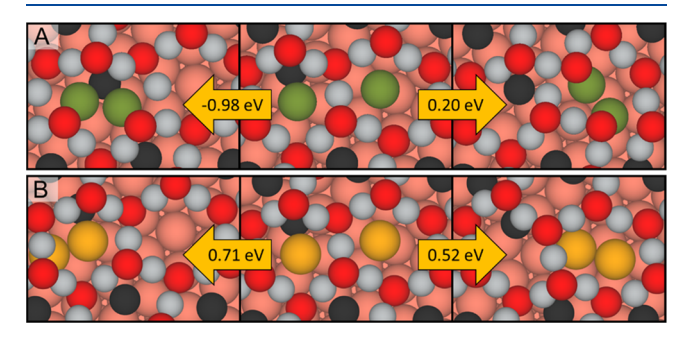


Figure 9. Reaction energy to aggregate Rh (A) and Pt (B) dimers on Site 15 (left) and Site 25 (right). The gold spheres represent Pt atoms while the color scheme for the other spheres is the same as that in Figure 5.

observed in the case of Pt dimers, even though the initial structure of these simulations was identical. Given that the metal adatom is not constrained within the oxide lattice, the migration pathway in which the adatom can maximize its coordination environment will involve moving it underneath the oxide, distorting the oxide layer during this process. The higher oxophilicity of Rh allows the bond breaking and bond forming with oxide-O to energetically compensate each other, thus facilitating higher mobility of Rh atoms across the cell as compared to Pt. This process is shown schematically in Figure 10. The relatively stronger interaction with O is also exhibited by the way oxide-O coordinates with the Rh dimer upon reconstruction (Figure 9).

To provide evidence that Rh atoms that have moved beneath the oxide layer and alloyed with the underling Cu(111) cannot be detected under STM, we have simulated nine hypothetical scenarios displayed in Figure 11. As shown in Figure 11A, the presence of atomically dispersed Rh induces a large bright area the size of the oxide ring. A one-to-one comparison of the simulated STM within our DFT-based model indicates that the brightest spots in the region are induced by electrons tunneling to the elevated up-O species that are within the same vicinity as the Rh located in the middle of the six-membered ring. When Rh is alloyed into the first or second layer of Cu(111), as shown in Figure 11B and C, the atomically dispersed Rh can no longer be detected. This is because the presence of the Rh alloy does not induce any local corrugation on the surface and is thus of the same height as the rest of the surface Cu atoms.

Charge State of Rh Active Sites and Surface Chemical **State in CO.** In order to determine the charge state of Rh on the oxide film we performed XPS. Figure 12A shows a comparison of the Rh $3d_{5/2}$ XPS peak of 1% Rh deposited on the "29" oxide film (blue) with that of 1% of a monolayer of Rh deposited on clean Cu(111) (red) as a reference for neutral Rh. The peaks overlap with each other almost perfectly at a binding energy (BE) of ~307 eV, consistent with the literature value for pure metallic Rh(111). And $3d_{5/2}$ components for various oxidized Rh species should appear between 307.8 and 310 eV. 42-45 The absence of any higher BE component (and in fact, the peak for Rh on the "29" oxide is very slightly narrower on the higher BE side than the one for Rh in Cu(111)) means that the Rh atoms on the "29" oxide are in a neutral charge state despite the presence of an oxide thin film, which tends to result in a cationic active site on a typical supported single atom catalyst. The fact that the "29" oxide layer is so thin that the Rh atoms are in contact with the underlying Cu(111) layer explains this result.

We then exposed the "29" oxide with and without Rh to 2×10^{-4} Torr of CO at 400 K and monitored the oxide O 1s peak using AP-XPS to evaluate the effect of Rh in the CO oxidation reaction on the rate of reduction of the oxide film. The "29" oxide O 1s peak area is plotted as a function of CO exposure time in Figure 12B. The reduction of the pristine "29" oxide proceeded relatively slowly and was completed after 210 min (black squares). The addition of 1% of a monolayer of Rh significantly accelerated the oxide reduction with completion observed after <70 min (blue circles), thus confirming the ability of Rh to catalyze the CO oxidation reaction. The C 1s spectra of the surface before and after reduction are shown in Figure 12C. The XPS spectrum of the as-deposited 1% Rh/Cu₂O surface shows the absence of adsorbed CO (spectrum (i)). Upon the initial exposure of the surface to 1×10^{-4} Torr

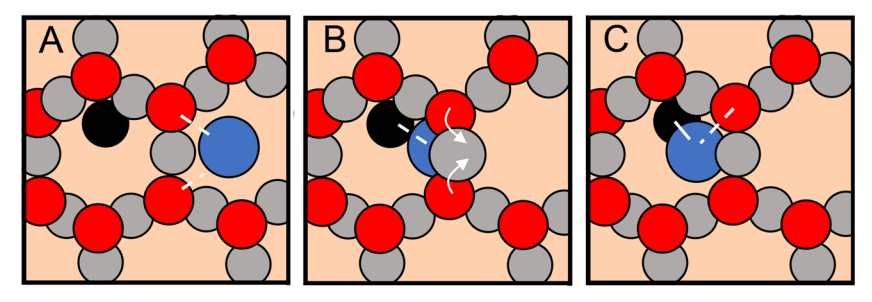


Figure 10. Schematic of how atom migration on the "29" oxide involves distortion of the oxide layer to maintain maximal coordination with the surface. For the adatom to move, it needs to break a bond with a surface O and form a bond with another surface O. Dotted lines, straight lines, and arrows denote weak interactions, strong interactions, and structural distortion directions, respectively. The spheres are color-coded: black (O-adatom), red (O-oxide), gray (Cu-oxide), blue (metal adatom). The atoms forming the Cu(111) surface beneath the oxide layer are omitted for clarity.

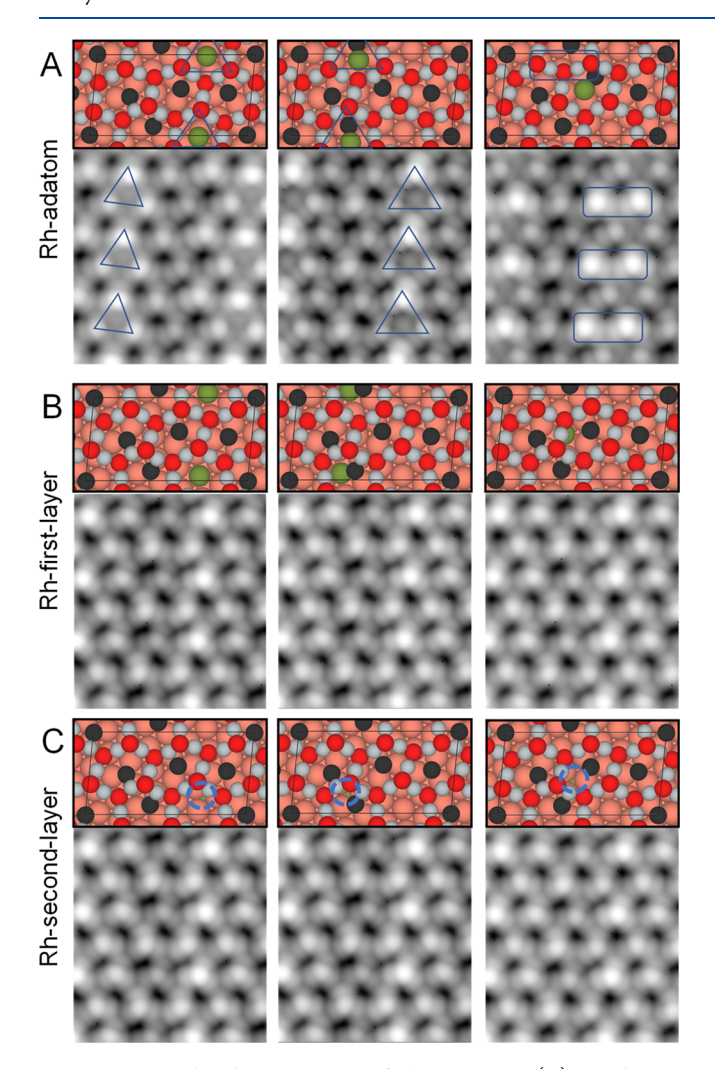


Figure 11. Simulated STM images of Rh_1 species as (A) an adatom, (B) a single-atom alloy in the first Cu(111) atomic layer, and (C) an alloyed atom in the second Cu(111) atomic layer, on three representative sites: within the empty ring, within a ring occupied by an O_{adatom} , and underneath the oxide ring. The color scheme for the spheres is the same as that in Figure 5. All images were simulated using a bias voltage of +1.5 V.

of CO at 300 K for 30 s, followed by pump down to UHV to probe the Rh sites, the peak for adsorbed CO appears, notably with two distinct components (spectrum (ii)). The main component at 286.2 eV is consistent with the BE for CO adsorbed on Rh(111) with the CO molecules bound atop the

Rh atoms, 40,41,46 suggesting that this peak comes from CO adsorbed on single Rh sites. The second, smaller component at 285.6 eV can be assigned to CO on Rh clusters since the BE is reasonably similar to the 285.4 eV BE of CO on threefold hollow sites of Rh(111). 40,41,46

Upon heating to 400 K in 2×10^{-4} Torr of CO to initiate the reduction process (spectrum (iii)), the lower BE component disappears, indicating that only atomically dispersed Rh species are detectable on the surface. This is consistent with the STM images showing the predominance of atomically dispersed Rh at 440 K, except the constant exposure to CO during the AP-XPS experiment likely prevented the migration of Rh atoms to below the oxide. After the reduction was complete and the sample cooled down to 300 K (spectrum (iv)), the single CO peak remains, and interestingly there is the growth of a broad peak at 283-285 eV. While it can be difficult to deconvolute various peaks that can contribute to this BE region, we can assign the higher BE side at ~284.2 eV to graphitic C and the lower BE component at ~283.3 eV to carbidic C. These C species are known products of CO dissociation, 47-49 thus confirming that CO dissociation occurred on the Rh/Cu₂O surface. As a comparison, the C 1s spectrum of the reduced pristine "29" oxide surface (spectrum (vi)) does not show a significant growth of any graphitic or carbidic C species under the same pressure and temperature conditions, although the exposure time to CO was three times longer than for the Rh/Cu₂O surface. This result demonstrates that the graphitic and carbidic C species could not have originated from any impurities in the CO gas or contamination desorbing from the chamber walls or from Xray induced dissociation of CO, and instead must have come from dissociation of CO on the Rh cluster sites.

CONCLUSIONS

We describe a well-defined model system consisting of Rh dispersed on the thin film "29" copper oxide grown on Cu(111). This model system enabled us to probe the CO oxidation reaction mechanism at the molecular scale via highly surface sensitive techniques; TPD, STM, and XPS. We discovered that Rh can catalyze the CO oxidation reaction on this reducible "29" copper oxide support, with CO_2 evolving from atomically dispersed Rh sites at a higher temperature than from Rh clusters. There are two pathways for this reaction as determined through TPD studies on an isotopically labeled oxide layer and confirmed with DFT. The first pathway involves the Mars—van Krevelen mechanism where a CO molecule adsorbs to an atomically dispersed Rh site and then

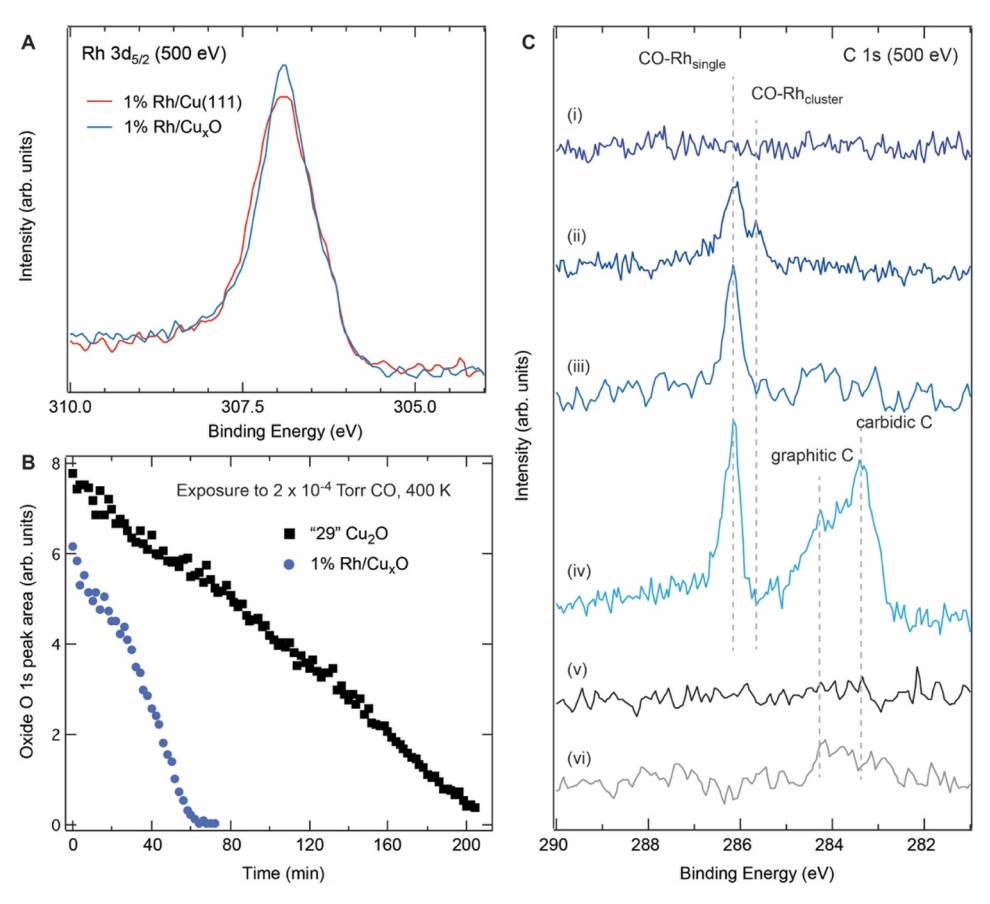


Figure 12. (A) Rh $3d_{5/2}$ XPS peak of 1% Rh deposited on Cu(111) (red) and 1% Rh deposited on the "29" oxide (blue). (B) Oxide O 1s peak area plotted as a function of exposure time to 2×10^{-4} Torr of CO at 400 K for the pristine "29" Cu₂O (black squares) and 1% Rh/Cu₂O (blue circles). (C) C 1s XPS spectra of (i) as-deposited 1% of a monolayer of Rh on the "29" Cu₂O structure, (ii) after exposure to 1×10^{-4} Torr of CO for 30 s at 300 K followed by pump down to UHV, (iii) at the first stage of reduction in 2×10^{-4} Torr of CO at 400 K, (iv) after the reduction in CO was complete and the sample was cooled down to 300 K. The C 1s spectra of the pristine "29" Cu₂O before (iv) and after (v) reduction in 2×10^{-4} Torr of CO at 400 K for 210 min are shown as a comparison.

extracts an O atom from the "29" oxide layer. The second pathway involves CO dissociation on a Rh cluster followed by oxidation of the resulting C atom by surface oxygen atoms as confirmed by isotope labeling. An overview schematic comparing the dynamics and species of the Rh-deposited surface with the Pt-deposited surface²² is shown in Figure 13. STM imaging revealed that once the reaction has completed,

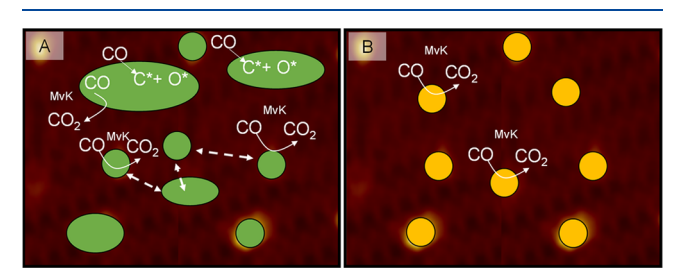


Figure 13. Overview schematic of CO oxidation on Rh vs Pt on the "29" thin film oxide including dynamical motion of the adatoms. (A) Rh-deposited "29" oxide contains both Rh atoms which catalyze CO oxidation via a Mars van Krevelen (MvK) mechanism and Rh clusters which can dissociate CO before oxidation. (B) Pt-deposited "29" oxide which contains only Pt atoms which are active for CO oxidation, but less so than Rh. Circles denote single atoms while larger ovals denote clusters of various sizes. Solid line arrows indicate a reaction step while dashed line arrows highlight adatom movement.

the Rh atoms move to sites under the oxide layer. Our results also demonstrate that the Rh on the "29" oxide exists in a neutral charge state, unlike most other supported single-atom catalysts. We bridge the pressure gap with ambient pressure studies on the same single crystal model systems and demonstrate that 1% of a monolayer of Rh on the "29" Cu₂O thin film significantly accelerates its reduction by CO at 400 K, thus confirming the ultrahigh vacuum surface science data. Together these results highlight the complexity of a chemical reaction occurring on a surface with a variety of ensembles that are often hard to differentiate between in high surface area catalysts studies and demonstrate how such well-defined single crystal experiments can deconvolute the different reaction pathways occurring on the different active sites.

ASSOCIATED CONTENT

Supporting Information

The Supporting Information is available free of charge at https://pubs.acs.org/doi/10.1021/acs.jpcc.2c02699.

DFT calculated CO oxidation reaction pathways and energetics. (PDF)

AUTHOR INFORMATION

Corresponding Authors

Iradwikanari Waluyo — National Synchrotron Light Source II, Brookhaven National Laboratory, Upton, New York 11973, United States; oorcid.org/0000-0002-4046-9722; Email: iwaluyo@bnl.gov

Jean-Sabin McEwen — The Gene and Linda Voiland School of Chemical Engineering and Bioengineering, Department of Physics and Astronomy, Department of Chemistry, and Department of Biological Systems Engineering, Washington State University, Pullman, Washington 99164, United States; Institute for Integrated Catalysis, Pacific Northwest National Laboratory, Richland, Washington 99352, United States; orcid.org/0000-0003-0931-4869; Email: js.mcewen@wsu.edu

E. Charles H. Sykes – Department of Chemistry, Tufts University, Medford, Massachusetts 02155, United States; orcid.org/0000-0002-0224-2084; Email: charles.sykes@tufts.edu

Authors

Alex C. Schilling – Department of Chemistry, Tufts University, Medford, Massachusetts 02155, United States Nisa Ulumuddin – The Gene and Linda Voiland School of Chemical Engineering and Bioengineering, Washington State University, Pullman, Washington 99164, United States

Volkan Çinar – Department of Chemistry, Tufts University, Medford, Massachusetts 02155, United States

Ryan T. Hannagan – Department of Chemistry, Tufts University, Medford, Massachusetts 02155, United States

Kyle Groden – The Gene and Linda Voiland School of Chemical Engineering and Bioengineering, Washington State University, Pullman, Washington 99164, United States

Yicheng Wang — Department of Chemistry, Tufts University, Medford, Massachusetts 02155, United States

Laura A. Cramer – Department of Chemistry, Tufts University, Medford, Massachusetts 02155, United States

Paul L. Kress – Department of Chemistry, Tufts University, Medford, Massachusetts 02155, United States

Dipna A. Patel – Department of Chemistry, Tufts University, Medford, Massachusetts 02155, United States

Beverly Vo – Department of Chemistry, Tufts University, Medford, Massachusetts 02155, United States

Adrian Hunt — National Synchrotron Light Source II, Brookhaven National Laboratory, Upton, New York 11973, United States; © orcid.org/0000-0002-5283-9647

Phillip Christopher – Department of Chemical Engineering, University of California, Santa Barbara, California 93106, United States; o orcid.org/0000-0002-4898-5510

Complete contact information is available at: https://pubs.acs.org/10.1021/acs.jpcc.2c02699

Author Contributions

OA.C.S. and N.U. contributed equally.

Notes

The authors declare no competing financial interest.

ACKNOWLEDGMENTS

Financial support for the experimental work at Tufts University was provided by the US Department of Energy, BES, Catalysis Science program under Contract No. DE-SC0021196. Financial support at Washington State University was provided

by the National Science Foundation CAREER program under Contract No. CBET-1653561. This work used the Extreme Science and Engineering Discovery Environment (XSEDE), 50 which is supported by National Science Foundation Grant Number ACI-1548562. Additional computer time for the computational work was performed using EMSL, a national scientific user facility sponsored by the Department of Energy's Office of Biological and Environmental Research and located at PNNL. PNNL is a multiprogram national laboratory operated for the US DOE by Battelle. Financial support at UCSB was provided by the US Department of Energy, BES, Catalysis Science program under Contract DE-SC0021124. This research used resources of the 23-ID-2 (IOS) beamline of the National Synchrotron Light Source II, a U.S. Department of Energy (DOE) Office of Science User Facility operated for the DOE Office of Science by Brookhaven National Laboratory under Contract No. DE-SC0012704.

REFERENCES

- (1) Beniya, A.; Higashi, S. Towards Dense Single-Atom Catalysts for Future Automotive Applications. *Nat. Catal.* **2019**, 2 (7), 590–602.
- (2) Thomas, J. M. The Concept, Reality and Utility of Single-Site Heterogeneous Catalysts (SSHCs). *Phys. Chem. Chem. Phys.* **2014**, *16* (17), 7647–7661.
- (3) Flytzani-Stephanopoulos, M.; Gates, B. C. Atomically Dispersed Supported Metal Catalysts. *Annu. Rev. Chem. Biomol. Eng.* **2012**, 3 (1), 545–574.
- (4) Liu, J. Catalysis by Supported Single Metal Atoms. ACS Catal. 2017, 7 (1), 34–59.
- (5) Yang, M.; Li, S.; Wang, Y.; Herron, J. A.; Xu, Y.; Allard, L. F.; Lee, S.; Huang, J.; Mavrikakis, M.; Flytzani-Stephanopoulos, M. Catalytically Active Au-O(OH) $_{\rm x}$ Species Stabilized by Alkali Ions on Zeolites and Mesoporous Oxides. *Science* **2014**, *346* (6216), 1498–1501
- (6) Yang, M.; Liu, J.; Lee, S.; Zugic, B.; Huang, J.; Allard, L. F.; Flytzani-Stephanopoulos, M. A Common Single-Site Pt(II)—O-(OH)_x— Species Stabilized by Sodium on "Active" and "Inert" Supports Catalyzes the Water-Gas Shift Reaction. *J. Am. Chem. Soc.* **2015**, 137 (10), 3470—3473.
- (7) Zhai, Y.; Pierre, D.; Si, R.; Deng, W.; Ferrin, P.; Nilekar, A. U.; Peng, G.; Herron, J. A.; Bell, B. D.; Saltsburg, H.; Mavrikakis, M.; Flytzani-Stephanopoulos, M. Alkali-Stabilized Pt-OH $_{\rm x}$ Species Catalyze Low-Temperature Water-Gas Shift Reactions. *Science* (80-.) **2010**, 329 (5999), 1633–1636.
- (8) Herzing, A. A.; Kiely, C. J.; Carley, A. F.; Landon, P.; Hutchings, G. J. Identification of Active Gold Nanoclusters on Iron Oxide Supports for CO Oxidation. *Science* (80-.) **2008**, 321 (5894), 1331–1335.
- (9) Shan, J.; Li, M.; Allard, L. F.; Lee, S.; Flytzani-Stephanopoulos, M. Mild Oxidation of Methane to Methanol or Acetic Acid on Supported Isolated Rhodium Catalysts. *Nature* **2017**, *551* (7682), 605–608.
- (10) Matsubu, J. C.; Yang, V. N.; Christopher, P. Isolated Metal Active Site Concentration and Stability Control Catalytic CO₂ Reduction Selectivity. *J. Am. Chem. Soc.* **2015**, *137* (8), 3076–3084.
- (11) Imai, S.; Miura, H.; Shishido, T. Selective Catalytic Reduction of NO with CO and C₃H₆ over Rh/NbOPO₄. *Catal. Today* **2019**, 332, 267–271.
- (12) Buchanan, D. A.; Hernandez, M. E.; Solymosi, F.; White, J. M. CO-Induced Structural Changes of Rh on TiO₂ Support. *J. Catal.* **1990**, *125* (2), 456–466.
- (13) Solymosi, F.; Erdöhelyi, A.; Bánsági, T. Methanation of CO₂ on Supported Rhodium Catalyst. *J. Catal.* **1981**, *68* (2), 371–382.
- (14) Guan, H.; Lin, J.; Qiao, B.; Miao, S.; Wang, A.-Q.; Wang, X.; Zhang, T. Enhanced Performance of Rh_1/TiO_2 Catalyst without Methanation in Water-Gas Shift Reaction. *AIChE J.* **2017**, *63* (6), 2081–2088.

- (15) Bliem, R.; van der Hoeven, J.; Zavodny, A.; Gamba, O.; Pavelec, J.; de Jongh, P. E.; Schmid, M.; Diebold, U.; Parkinson, G. S. An Atomic-Scale View of CO and H₂ Oxidation on a Pt/Fe₃O₄ Model Catalyst. *Angew. Chemie Int. Ed.* **2015**, 54 (47), 13999–14002.
- (16) Parkinson, G. S.; Novotny, Z.; Argentero, G.; Schmid, M.; Pavelec, J.; Kosak, R.; Blaha, P.; Diebold, U. Carbon Monoxide-Induced Adatom Sintering in a Pd-Fe₃O₄ Model Catalyst. *Nat. Mater.* **2013**, *12* (8), 724–728.
- (17) Hulva, J.; Meier, M.; Bliem, R.; Jakub, Z.; Kraushofer, F.; Schmid, M.; Diebold, U.; Franchini, C.; Parkinson, G. S. Unraveling CO Adsorption on Model Single-Atom Catalysts. *Science* (80-.) **2021**, 371 (6527), 375–379.
- (18) Kraushofer, F.; Resch, N.; Eder, M.; Rafsanjani-Abbasi, A.; Tobisch, S.; Jakub, Z.; Franceschi, G.; Riva, M.; Meier, M.; Schmid, M.; et al. Surface Reduction State Determines Stabilization and Incorporation of Rh on α -Fe₂O₃(1 $\overline{1}$ 02). *Adv. Mater. Interfaces* **2021**, 8 (8), 2001908.
- (19) Wang, Y. G.; Mei, D.; Glezakou, V. A.; Li, J.; Rousseau, R. Dynamic Formation of Single-Atom Catalytic Active Sites on Ceria-Supported Gold Nanoparticles. *Nat. Commun.* **2015**, *6*, 1–8.
- (20) Liu, L.; Meira, D. M.; Arenal, R.; Concepcion, P.; Puga, A. V.; Corma, A. Determination of the Evolution of Heterogeneous Single Metal Atoms and Nanoclusters under Reaction Conditions: Which Are the Working Catalytic Sites? *ACS Catal.* **2019**, 9 (12), 10626–10639.
- (21) Therrien, A. J.; Zhang, R.; Lucci, F. R.; Marcinkowski, M. D.; Hensley, A.; McEwen, J.-S.; Sykes, E. C. H. Structurally Accurate Model for the "29"-Structure of Cu_xO/Cu(111): A DFT and STM Study. *J. Phys. Chem. C* **2016**, *120* (20), 10879–10886.
- (22) Therrien, A. J.; Hensley, A. J. R.; Marcinkowski, M. D.; Zhang, R.; Lucci, F. R.; Coughlin, B.; Schilling, A. C.; McEwen, J.-S.; Sykes, E. C. H. An Atomic-Scale View of Single-Site Pt Catalysis for Low-Temperature CO Oxidation. *Nat. Catal.* **2018**, *1* (3), 192–198.
- (23) Hensley, A. J. R.; Therrien, A. J.; Zhang, R.; Marcinkowski, M. D.; Lucci, F. R.; Sykes, E. C. H.; McEwen, J.-S. CO Adsorption on the "29" Cu_xO/Cu(111) Surface: An Integrated DFT, STM, and TPD Study. *J. Phys. Chem. C* **2016**, *120* (44), 25387–25394.
- (24) Hannagan, R. T.; Patel, D. A.; Cramer, L. A.; Schilling, A. C.; Ryan, P. T. P. P.; Larson, A. M.; Çınar, V.; Wang, Y.; Balema, T. A.; Sykes, E. C. H. Combining STM, RAIRS and TPD to Decipher the Dispersion and Interactions Between Active Sites in RhCu Single-Atom Alloys. *ChemCatChem.* **2020**, *12* (2), 488–493.
- (25) Kolasinski, K. W. Surface Science: Foundations of Catalysis and Nanoscience 2012, DOI: 10.1002/9781119941798.
- (26) Simonovis, J. P.; Hunt, A.; Palomino, R. M.; Senanayake, S. D.; Waluyo, I. Enhanced Stability of Pt-Cu Single-Atom Alloy Catalysts: In Situ Characterization of the Pt/Cu(111) Surface in an Ambient Pressure of CO. *J. Phys. Chem. C* **2018**, 122 (8), 4488–4495.
- (27) Kresse, G.; Furthmüller, J. Efficient Iterative Schemes for *Ab Initio* Total-Energy Calculations Using a Plane-Wave Basis Set. *Phys. Rev. B* **1996**, 54 (16), 11169–11186.
- (28) Kresse, G.; Hafner, J. Ab Initio Molecular Dynamics for Liquid Metals. *Phys. Rev. B* **1993**, *47* (1), 558–561.
- (29) Lejaeghere, K.; Bihlmayer, G.; Björkman, T.; Blaha, P.; Blügel, S.; Blum, V.; Caliste, D.; Castelli, I. E.; Clark, S. J.; Dal Corso, A.; et al. Reproducibility in Density Functional Theory Calculations of Solids. *Science* (80-.) **2016**, 351 (6280), aad3000.
- (30) Kresse, G.; Joubert, D. From Ultrasoft Pseudopotentials to the Projector Augmented-Wave Method. *Phys. Rev. B Condens. Matter Mater. Phys.* **1999**, *59* (3), 11–19.
- (31) Perdew, J. P.; Burke, K.; Ernzerhof, M. Generalized Gradient Approximation Made Simple. *Phys. Rev. Lett.* **1996**, 77 (18), 3865–3868.
- (32) Feibelman, P. J. Surface-Diffusion Mechanism versus Electric Field: Pt/Pt(001). Phys. Rev. B Condens. Matter Mater. Phys. 2001, 64 (12), 1–6.
- (33) Monkhorst, H. J.; Pack, J. D. Special Points for Brillouin-Zone Integrations. *Phys. Rev. B* **1976**, *13* (12), 5188–5192.

- (34) Henkelman, G.; Uberuaga, B. P.; Jónsson, H. A Climbing Image Nudged Elastic Band Method for Finding Saddle Points and Minimum Energy Paths. *J. Chem. Phys.* **2000**, *113* (22), 9901–9904.
- (35) Sheppard, D.; Terrell, R.; Henkelman, G. Optimization Methods for Finding Minimum Energy Paths. *J. Chem. Phys.* **2008**, 128 (13), 134106.
- (36) Filot, I. A. W.; Shetty, S. G.; Hensen, E. J. M.; Van Santen, R. A. Size and Topological Effects of Rhodium Surfaces, Clusters and Nanoparticles on the Dissociation of CO. *J. Phys. Chem. C* **2011**, *115* (29), 14204–14212.
- (37) de Koster, A.; van Santen, R. A. Dissociation of CO on Rh Surfaces. Surf. Sci. 1990, 233 (3), 366–380.
- (38) De Mongeot, F. B.; Toma, A.; Molle, A.; Lizzit, S.; Petaccia, L.; Baraldi, A. Carbon Monoxide Dissociation on Rh Nanopyramids. *Phys. Rev. Lett.* **2006**, 97 (5), 1–4.
- (39) Ligthart, D. A. J. M.; Filot, I. A. W.; Almutairi, A. A. H.; Hensen, E. J. M. Identification of Step-Edge Sites on Rh Nanoparticles for Facile CO Dissociation. *Catal. Commun.* **2016**, *77*, 5–8.
- (40) Beutler, A.; Lundgren, E.; Nyholm, R.; Andersen, J. N.; Setlik, B.; Heskett, D. On the Adsorption Sites for CO on the Rh(111) Single Crystal Surface. *Surf. Sci.* **1997**, *371* (2–3), 381–389.
- (41) Beutler, A.; Lundgren, E.; Nyholm, R.; Andersen, J. N.; Setlik, B. J.; Heskett, D. Coverage- and Temperature-Dependent Site Occupancy of Carbon Monoxide on Rh(111) Studied by High-Resolution Core-Level Photoemission. *Surf. Sci.* **1998**, *396* (1–3), 117–136.
- (42) Abe, Y.; Kato, K.; Kawamura, M.; Sasaki, K. Rhodium and Rhodium Oxide Thin Films Characterized by XPS. *Surf. Sci. Spectra* **2001**, 8 (2), 117–125.
- (43) Force, C.; Román, E.; Guil, J. M.; Sanz, J. XPS and ¹H NMR Study of Thermally Stabilized Rh/CeO₂ Catalysts Submitted to Reduction/Oxidation Treatments. *Langmuir* **2007**, 23 (8), 4569–4574.
- (44) Kim, S. M.; Qadir, K.; Seo, B.; Jeong, H. Y.; Joo, S. H.; Terasaki, O.; Park, J. Y. Nature of Rh Oxide on Rh Nanoparticles and Its Effect on the Catalytic Activity of CO Oxidation. *Catal. Lett.* **2013**, 143 (11), 1153–1161.
- (45) Kibis, L. S.; Stadnichenko, A. I.; Koscheev, S. V.; Zaikovskii, V. I.; Boronin, A. I. XPS Study of Nanostructured Rhodium Oxide Film Comprising Rh⁴⁺ Species. *J. Phys. Chem. C* **2016**, *120* (34), 19142–19150.
- (46) Garcia-Martinez, F.; Schiller, F.; Blomberg, S.; Shipilin, M.; Merte, L. R.; Gustafson, J.; Lundgren, E.; Ortega, J. E. CO Chemisorption on Vicinal Rh(111) Surfaces Studied with a Curved Crystal. *J. Phys. Chem. C* **2020**, *124* (17), 9305–9313.
- (47) Nakamura, J.; Toyoshima, I.; Tanaka, K. Formation of Carbidic and Graphite Carbon from CO on Polycrystalline Cobalt. *Surf. Sci.* **1988**, *201* (1), 185–194.
- (48) Genuzio, F.; Genoni, P.; Menteş, T. O.; Santos, B.; Sala, A.; Lenardi, C.; Locatelli, A. Stimulated CO Dissociation and Surface Graphitization by Microfocused X-Ray and Electron Beams. *J. Phys. Chem. C* **2019**, *123* (13), 8360–8369.
- (49) Wu, C. H.; Eren, B.; Bluhm, H.; Salmeron, M. B. Ambient-Pressure X-Ray Photoelectron Spectroscopy Study of Cobalt Foil Model Catalyst under CO, H₂, and Their Mixtures. *ACS Catal.* **2017**, 7 (2), 1150–1157.
- (50) Towns, J.; Cockerill, T.; Dahan, M.; Foster, I.; Gaither, K.; Grimshaw, A.; Hazlewood, V.; Lathrop, S.; Lifka, D.; Peterson. XSEDE: Accelerating Scientific Discovery. *Comput. Sci. Eng.* **2014**, *16* (5), 62.